Additive-Free Synthesis of (Chiral) Gold Bipyramids from Pentatwinned Nanorods

Francisco Bevilacqua, Robin Girod, Victor F. Martín, Manuel Obelleiro-Liz, Gail A. Vinnacombe-Willson, Kyle Van Gordon, Johan Hofkens, Jose Manuel Taboada, Sara Bals, and Luis M. Liz-Marzán*

Read Online

ACCESS | Metrics & More | Article Recommendations | Supporting Information

ABSTRACT: The production of colloidal metal nanostructures with complex geometries usually involves shape-directing additives, such as metal ions or thiols, which stabilize high-index facets. These additives may however affect the nanoparticles' surface chemistry, hindering applications, e.g., in biology or catalysis. We report herein the preparation of gold bipyramids with no need for additives and shape yields up to 99%, using pentatwinned Au nanorods as seeds and cetyltrimethylammonium chloride as surfactant. For high-growth solution:seed ratios, the bipyramids exhibit an unusual "belted" structure. Three-dimensional electron microscopy revealed the presence of high-index $\{117\}$, $\{115\}$, and $\{113\}$ side facets, with $\{113\}$ and $\{112\}$ facets at the belt. Belted bipyramids exhibit strong near-field enhancement and high extinction in the near-infrared, in agreement with electromagnetic simulations. These Ag-free bipyramids were used to seed chiral overgrowth using 1,1′-binaphthyl-2,2′-diamine as a chiral inducer, with g-factor up to 0.02, likely the highest reported for bipyramid seeds so far.
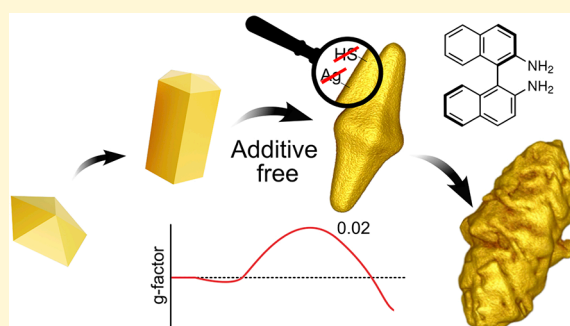
Various fabrication methods have enabled the reliable fabrication of both anisotropic and asymmetric (chiral) noble metal nanoparticles, with potential applications in various fields such as sensing,[1,2] imaging,[3,4] and nanomedicine.[5,6] Distinct optical properties in such materials arise from localized surface plasmon resonances (LSPRs), which result in high absorption and scattering cross-sections in the visible and near IR (NIR). Such optical properties, including LSPR wavelength and the strength of near-field interactions, depend on nanoparticle composition, shape, and size, as well as on the dielectric environment.[7] Inherently chiral plasmonic nanomaterials offer new opportunities to develop functional materials with strong, tunable, and specific interactions with circularly polarized light, which could be leveraged e.g. for enantioselective catalysis and biosensing.[2] Overall, gold is frequently the preferred choice for many applications because of its higher chemical stability, optical tunability in the visible and NIR, and biocompatibility.

Colloidal seed-mediated nanoparticle synthesis has been shown to direct crystal growth into different geometries, depending on the crystallinity of the seeds and the presence of "shape-directing" species such as metal salts or surfactants.[8] As surfactants are needed for nanoparticle growth and stabilization, we consider "additives" any other chemical species that may be used to affect crystal growth. Seed preparation is therefore a key step, especially for the growth of uniform gold nanorods (NRs) and bipyramids (BPs).[9−11] Although single crystalline (SC)-NRs are readily prepared from SC Au seeds (in the presence of Ag^+ ions),[10,12] Ag-free Au pentatwinned (PT)-NRs require decahedral seeds presenting five twin planes, which propagate during growth into a pentagonal prism-like morphology. The addition of Ag^+ as a shape-directing reagent is similarly required for the growth of Au PT BPs. Even though the preparation of PT nanoparticles often suffers from contamination with other morphologies (often due to poor twinning yield within the seeds), recent improvements have demonstrated twinning efficiencies up to 98%.[13,14] This significant increase in the yield of PT seeds enables more extensive studies on PT morphologies such as decahedrons, PT-NRs, and BPs.[15,16] Apart from the absence or presence of crystalline defects in SC or PT nanocrystals, they also differ in their surface facet Miller indices. For instance, SC-NRs feature high-index $\{520\}$ lateral facets and a combination of $\{100\}$, $\{110\}$, and $\{111\}$ facets at the tips,[17,18] whereas PT-NRs are enclosed by five $\{100\}$ lateral facets and ten $\{111\}$ tip facets.[19]

Albeit less popular, Au BPs are attractive alternatives to NRs, capable of exhibiting higher-quality plasmon bands,[20] stronger near-field enhancements,[21] as well as higher sensitivity to refractive index changes in the surrounding medium.[22] The geometry of these particles consists of two elongated pyramids with pentagonal cross-section, joining at a common base plane. PT seeds are decahedral, thus enclosed by ten {111} facets.[23] During growth into bipyramids, the particle is elongated in the <110> direction, with the seed staying at the center.[13] Although the role of silver remains unclear, it seems to reduce the growth rate along the {100} and {110} facets, while favoring the development of higher index facets.[24] Most crystallographic studies report indices in the {11n} family, i.e., {115}, {113}[20,25−27] on the side facets, with higher indices less often reported.[20] Lower index {100} and {111} facets are still reported at the center and at the tips, respectively. The presence of high index facets shows potential interest in the development of more efficient catalysts.[28]

Regarding silver content, 3−4 wt % has been reported for Au BPs, mostly localized at/near the surface, thereby modifying their surface chemistry.[29] Silver-free preparation of BPs is also reported in the literature. One example uses salicylate and H_2PdCl_4 as additives,[30] whereas a most recent one uses a racemic mixture of *L/D* cysteine.[16] Both preparations show intriguing structures of BPs with unusual rounded structures.[16,30] In general, for BPs above *ca.* 200 nm, stair-like, rough facets with high indices ({910} and {730}) have also been reported.[13,14,31] Additionally, some studies report the possibility of overgrowing BPs into different geometries such as dumbbell shapes, rods, or larger bipyramids, using different surfactants.[20] For example, concave bipyramids were obtained by the overgrowth of BPs in the presence of cetyltributy-lammonium bromide and silver nitrate.[32]

The increased knowledge of the surface chemistry of Au nanoparticles has pushed forward investigations of these materials as seeds for the preparation of chiral nanomaterials. Previous investigations on the preparation of chiral plasmonic particles employed chiral biomolecules, such as cysteine and glutathione, to induce chiral overgrowth on cubes or octahedra.[33] Cysteine was also used for chiral growth on Au SC-NRs, resulting in chiral NRs with interesting 4-fold symmetries.[34] On the other hand, by using the cosurfactant 1,1′-binaphthyl-2,2′-diamine (BINAMINE) as a chirality-inducing agent, Au SC-NRs covered by chiral wrinkled geometries were obtained.[35,36] More recently, PT-NRs, BPs, and decahedra have also been used as seeds, showing different morphological evolution during chiral growth,[37−40] even with inverted handedness resulting from chiral growth on PT- and SC-NRs, while using the same enantiomer of the chiral inducer.[37,38]

We report herein an unusual additive-free overgrowth of Au PT-NRs, which allows the formation of large BPs (up to ca. 330 nm × 170 nm) with smooth facets. Interestingly, in the larger BPs we consistently observe the formation of a pronounced "belt" at the BP central plane. We stress that the synthetic process is entirely free of additives that might ultimately affect the surface chemistry of the BPs (such as other metal ions or thiols/cosurfactants), rendering these particles particularly interesting for various applications (*e.g.*, biomedical, where Ag^+ can induce cytotoxicity).[41] In the context of chiral overgrowth, silver-free surfaces are also usually preferred.[39,40]

The synthesis protocol comprises three main steps, namely, (*i*) PT seed formation, followed by (*ii*) their overgrowth into PT-NRs, and (*iii*) overgrowth of PT-NRs into PT-BPs, as schematically shown in Supporting Information (SI) Figure S1. The first and second steps are based on our previous report on the synthesis of PT-NRs,[13] including the seed aging and postsynthetic purification of Au PT-NRs by depletion forces (see details and additional characterization in the Supporting Information, Table S1 and Figures S1 and S2). Although the growth of Au BPs from small seeds relies on the use of CTAB as a shape-directing surfactant,[13] the overgrowth of PT-NRs into BPs was found to work best in the presence of the chloride
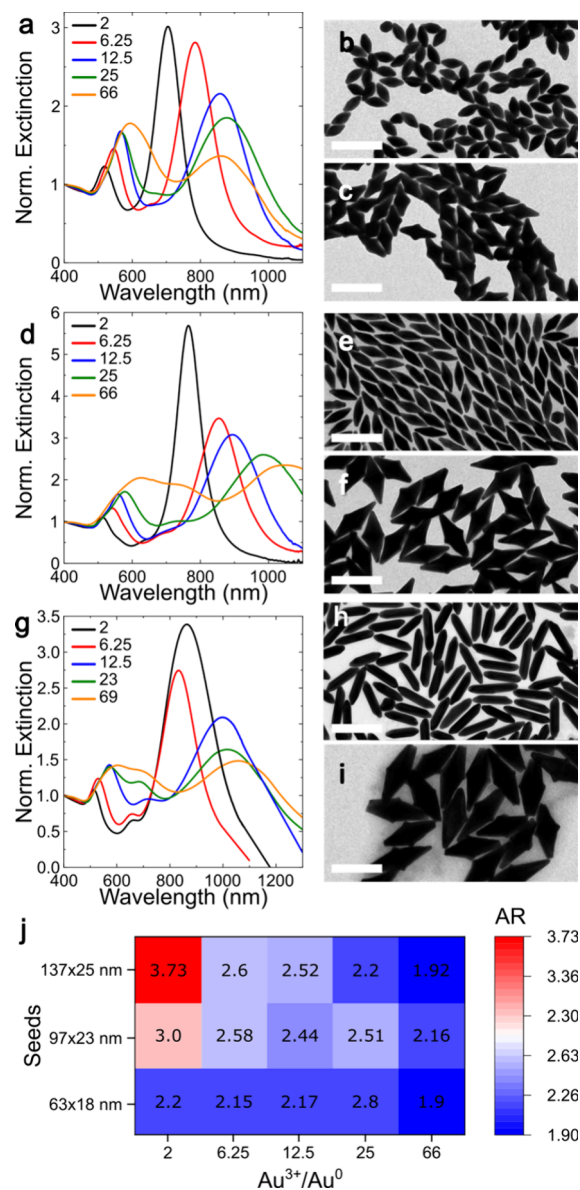
Figure 1. Overgrowth on Au PT-NRs with different sizes and varying $[Au^{3+}]/[Au^0]$ ratios. UV−vis−NIR spectra normalized at 400 nm (a, d, g) and TEM images (b−i) for two selected molar ratios (2 and 12.5) are shown for the overgrowth on small (a−c), medium (d−f), and large (g−i) Au PT-NRs. The $[Au^{3+}]/[Au^0]$ ratios for each spectrum are indicated in the legends. Scale bars in TEM images: 200 nm. (j) Heat map of the aspect ratio (AR) evolution for the various Au PT-NR seeds, depending on the growth ratio.
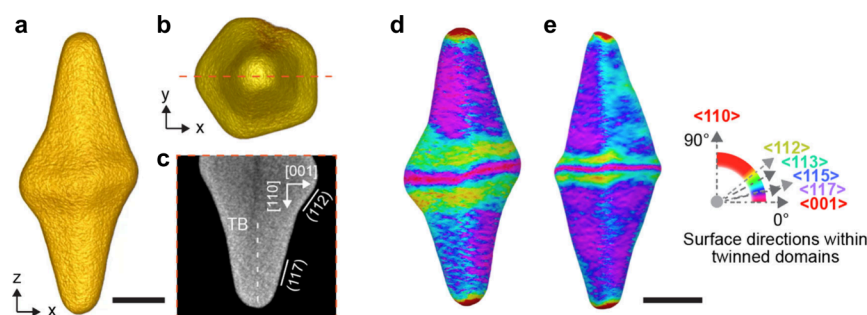
Figure 2. Structural characterization of "belted" bipyramids. (a, b) Isosurface rendering of an electron tomography reconstruction of a bipyramid prepared from medium Au PT-NRs, with a growth ratio of $[Au^{3+}]/[Au^0] = 6.25$. An animation is provided as Supporting Information Movie S1. (c) Orthoslice through the 3D reconstruction, extracted along the dotted line in panel b, showing the central twin boundary (TB) as a darker line. This enables identification of the crystal directions within twinned domains and indexing of the lateral and belt facets based on their angles with the vertical axis. (d, e) Surface analysis of particles prepared from medium NRs, with growth ratios of $[Au^{3+}]/[Au^0] = 6.25$ (d) and $[Au^{3+}]/[Au^0] = 12.5$ (e). Color coding corresponds to the angle of the surface normal vectors with respect to the vertical ⟨110⟩ axis, which can be related to crystal directions within twinned domains. Scale bars are 30 nm (a−d) and 50 nm (e).

counterpart (CTAC). In a typical preparation, BP overgrowth involves adding the gold precursor to a mixture of ascorbic acid (AA), Au PT-NR seeds, and CTAC, at 30 °C. Compared to CTAB, CTAC exhibits weaker adsorption on the gold surface,[24] and therefore is often used to prepare isotropic geometries such as larger spheres.[42]

We thus expected that CTAC would facilitate uniform NP growth, i.e., similar growth rate along all crystallographic directions.[24,42] Although no significant effects could be observed by varying the AA/Au³⁺ molar ratio, the BP morphology appeared less well-defined at high ratios (e.g., AA/Au³⁺ = 10, Figure S3). We did observe a strong influence of CTAC concentration and temperature, with wide morphology variations in the ranges of 25−100 mM CTAC and 15−45 °C (Figure S4). Optimal bipyramidal shapes were obtained at 25 mM CTAC and 30 °C. Even though for a more efficient analysis of the synthesis process we chose to work with 10 mL aliquots, the same process can be scaled-up to at least 100 mL with no loss of shape yield (Figure S5).

The generality of the process was explored by using Au PT-NRs of three different sizes and different molar ratios between the growth solution and Au PT-NR seeds: $[Au^{3+}]/[Au^0]$. The initial Au PT-NR seeds were defined according to their dimensions as small (63 nm × 18 nm), medium (97 nm × 23 nm), and large (137 nm × 25 nm); representative transmission electron microscopy (TEM) images and UV−vis−NIR spectra are shown in Figure S1. As described in the Materials and Methods section (Supporting Information), the concentration of seeds was estimated from the absorbance at 400 nm, which relates to the concentration of Au⁰.[43] It should be noted, however, that this approach is not accurate for large Au NPs due to increased light scattering, but was considered sufficient to identify common features among various syntheses. Overall, BPs of different sizes and aspect ratios were obtained, with smaller seeds producing smaller BPs with lower aspect ratios, and *vice versa* (Figure 1; Table S2). For each seed size, $[Au^{3+}]/[Au^0]$ ratios between 2 and 66 were applied for overgrowth. In all three series, redshift and broadening of the LSPR bands were observed as $[Au^{3+}]/[Au^0]$ was increased (Figure 1a,d,g; Table S2). For a low $[Au^{3+}]/[Au^0]$ ratio of 2, the recorded LSPR maxima (700−860 nm) were blue-shifted with respect to those of the corresponding Au PT-NR seeds, in agreement with the decrease of aspect ratio measured by TEM (see Tables S1 and S2). TEM characterization for this ratio

additionally revealed the formation of elongated BPs with pointy tips, but with a rounded body, featuring less defined edges (Figure 1b,e,h). This effect is more evident when using large PT-NR seeds (Figure 1h). However, when increasing the $[Au^{3+}]/[Au^0]$ ratio, the LSPR red-shifted accordingly (Figure 1a,d,g). For higher growth ratios above *ca.* 6, the BPs exhibited better defined edges and a "belt" structure around the center of the particle (Figures 1c,f,i and S6 and S7). SEM characterization confirmed that particles are uniform in their shape and belted structure (Figures S8 and S9). In general, the aspect ratio decreases at high growth ratios, as illustrated by a heat map in Figure 1j, showing convergence into values close to 2. This result means that BPs of different dimensions but with similar aspect ratios can be prepared. Overall, yields of BP morphology up to ~99% were measured for $[Au^{3+}]/[Au^0] \leq$ 25, but decreased to ~80% for excessive overgrowth. This lower yield at high ratios is accompanied by extensive tip truncation, likely due to favored growth on the lateral BP facets. Tip truncation is more obvious for longer PT-NR seeds (*e.g.*, $[Au^{3+}]/[Au^0] = 12.5$, Figure 1i), whereas it only occurs at higher $[Au^{3+}]/[Au^0]$ values for shorter seeds (*e.g.*, $[Au^{3+}]/[Au^0] > 25$, Figure S6d,e).

For a detailed characterization of this unusual, belted structure, we employed electron tomography based on tilt series of high-angle annular dark field scanning TEM (HAADF-STEM) images.[44] Panels a and b of Figure 2 show two orientations of a three-dimensional (3D) isosurface rendering of an electron tomography reconstruction, for a representative BP prepared from medium (97 nm × 23 nm) Au PT-NRs with $[Au^{3+}]/[Au^0] = 6.25$. Viewed along the long axis, the reconstruction confirmed that the 5-fold symmetry and therefore the pentatwinned structure is preserved in the final particles (Figure 2b). Additionally, the 3D reconstruction of the particles allowed us to identify the nature of the various facets, as well as internal lattice defects (central twin boundary, TB, Figure 2c). By measuring the surface angles with respect to the central twinning axis, crystallographic indices can be proposed for the different surface facets within twinned domains (see SI Materials and Methods and Figure 2c−e). Although similar angle dependence measurements are commonly used for the identification of different facets using 2D NP projections,[16,26] the use of a 3D reconstruction allows us to visualize the different facets in space. Interestingly, high-index facets of type {11n} were identified. The pyramidal sides
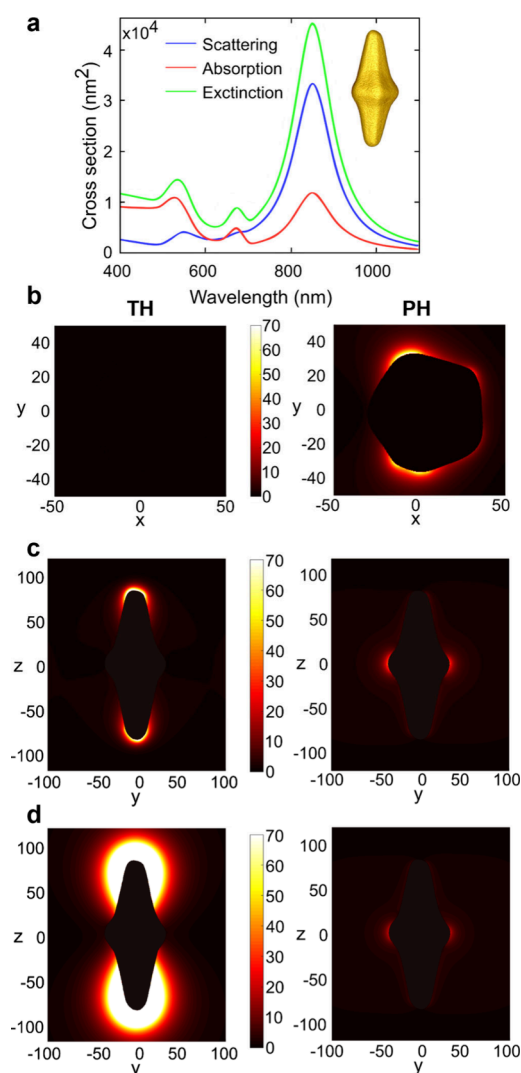
Figure 3. Electromagnetic simulation using as a model the electron tomography reconstruction of the belted BP shown in Figure 2. (a) Simulated scattering (blue), absorption (red), and extinction (green) cross-sections. The inset shows the tomography reconstruction of the particle used for the simulations. (b−d) Near-field enhancement maps for the same belted particle, illuminated at different wavelengths of 525 (b), 675 (c), and 850 nm (d). Left panels show the x,y-plane; right panels show the y,z-plane; Light polarization is in the transverse direction (TH) and parallel direction (PH), respectively.

are typically flat and dominated by one of {113}, {115}, or {117} facets (Figure 2d,e). The central belt comprises a combination of {112} and {113} facets, and the tips are typically rounded or with facets close to {111}. Similar results were observed at higher $[Au^{3+}]/[Au^0]$ = 12.5 (Figure 2e). Remarkably, despite the lack of silver as a shape-directing agent, we obtained similar crystallographic facets as those typically reported for Ag-assisted syntheses.[20,27] The absence of Ag in the final particles was confirmed by energy dispersion X-ray spectroscopy (EDS), as shown in Figure S10. It should also be mentioned that similar belted BPs were recently reported, but always requiring the addition of additives, such as H_2PdCl_4, salicylate or cysteine.[16,30]

Regarding the optical properties, it was interesting to note that, whereas BPs were produced in high shape yield (∼99%), the ratio between the extinction of longitudinal and transverse
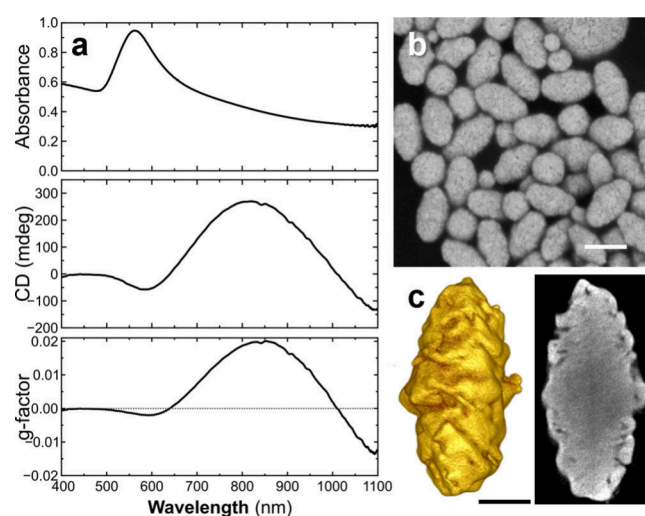
Figure 4. (a) UV−vis, CD, and g-factor spectra for chiral particles grown from medium BPs (see text for details), with an $[Au^{3+}]/[Au^0]$ ratio of 3. (b) Representative SEM image of the wrinkled BPs. Scale bar is 200 nm. (c) Electron tomography reconstruction (left) and central orthoslice (right) of a selected chiral BP, scale bar is 50 nm. An animation is provided as Supporting Information Movie S6.

bands is lower than typical values for silver-assisted BPs (Table S2).[13] To understand this unusual result, electromagnetic simulations were carried out using the method of moments (MoM).[35,45] This methodology is particularly accurate for solving scattering problems because it uses Green's functions and its derivatives. Greater accuracy is obtained because we use a 3D reconstruction from electron tomography as the input model in the simulations. The calculated extinction, absorption, and scattering cross-section spectra (Figure 3a) clearly show that the longitudinal band is dominated by scattering, whereas the major contribution to other modes is absorption. Although the position of the longitudinal band is not strongly influenced by the presence of the belt, a small blue-shift is observed due to the belt, compared to "ideal" BPs with similar dimensions (Figure S11). The belted bipyramids are observed to have a more intense transverse band and a reduced longitudinal intensity, leading to the observed lower ratio. Electromagnetic simulations also allowed us to identify the nature of the various plasmon modes (Figure 3b−d). Under irradiation at 525 nm (Figure 3b; SI Movie S2) a transverse dipolar feature is clearly observed. Interestingly, when compared to a nonbelted bipyramid, the enhancement is observed to be more distributed over the whole belt (SI Figure S12 and Movie S3). However, for the lower intensity band at 675 nm we can see (Figure 3c; SI Movie S4) enhancement both at the belt and the tips, depending on the polarization of incident light, which we identify as corresponding to a multipolar mode. Finally, for the mode at 850 nm (Figure 3d; SI Movie S5), a dipolar longitudinal character is clearly observed, as usual for Au BPs, with strong near-field enhancement at the tips. One can note that the enhancement under transverse polarized light is strongly localized at the tips for belted particles, whereas the enhancement is more distributed on the sides when the belt is not present.

We finally explored one of the benefits of growing Ag-free BPs, related to their potential use as seeds for further chiral growth. Even though chiral growth on both Au SC-NRs and

BPs has been reported,[38−40] the results indicate that the presence of Ag on the surface was detrimental to chiral growth. This is the case for the growth of chiral wrinkles in the presence of BINAMINE.[35] We thus tested *S*-BINAMINE-induced chiral growth on our Ag-free BPs. We selected BPs prepared from medium PT-NRs with $[Au^{3+}]/[Au^0]$ = 6.25, to which an appropriate growth solution was added,[35] with $[Au^{3+}]/[Au^0]$ ratios ranging from 1 to 5 (additional information about these samples can be found in SI Figure S13). Summarized in Figure 4a is the optical and morphological characterization of the particles resulting from chiral overgrowth of medium BPs, with $[Au^{3+}]/[Au^0]$ = 3. The UV−vis−NIR spectrum shows maximum absorbance at 563 nm and a tail over the whole range up to 1100 nm, resembling the usual results for wrinkled Au NRs. Both circular dichroism (CD) and *g*-factor spectra in Figure 4a display a broad positive band around 820 nm, with a second negative feature at higher (NIR) wavelengths that could not be recorded in our instrument. This result is in agreement with a previous report for *S*-BINAMINE-induced chiral PT-NRs, showing inverted handedness compared to SC-NR seeds.[38] In this sample, a maximum *g*-factor of 0.02 was obtained, which is below the best values for other chiral NRs, but still significantly higher (by one order of magnitude) than the values reported for cysteine and glutathione-induced chiral BPs.[39,40] Both SEM and electron tomography (Figure 4b,c) confirmed the presence of wrinkled features around a central BP. Although some secondary nucleation could be observed in this sample, most of the particles maintain the elongated shape dictated by the BP seeds. The high resolution provided by electron tomography evidence the formation of thin, tilted wrinkles (Figure 4c) and preservation of the 5-fold symmetry during the growth (Figure S14). These results enable further opportunities to tune the overall size and the fine details of chiral features on Au BPs, with the corresponding optimization of the chiroptical response. A control experiment for chiral overgrowth on Au BPs prepared in the presence of silver (Figure S15),[13] evidenced hindered chiral overgrowth using similar conditions, with poor optical response and moderate or even no wrinkling (Figure S16).

In summary, we have introduced an efficient synthesis route toward the preparation of Ag-free Au bipyramids. This synthesis has the advantage of not requiring the use of any additives that might affect the surface chemistry and applications of Au BPs. The method offers wide flexibility in terms of particle size and aspect ratio, which can be tuned through the dimensions of the PT-NR seeds and the concentration of the growth solution. The stabilization of high-index facets in the absence of silver challenges some of the currently proposed growth mechanisms and offers possibilities for catalysis or sensing. Finally, we also demonstrated efficient and simple chiral overgrowth in the presence of BINAMINE/CTAC, which is also facilitated by the absence of Ag on the BP surface. Wide opportunities arise for optimization of chiral morphologies and for reaching higher *g*-factors, either with the same or other chiral inducers, such as amino acids or peptides.

■ ASSOCIATED CONTENT

ⓢ Supporting Information

The Supporting Information is available free of charge at https://pubs.acs.org/doi/10.1021/acsmaterialslett.4c01605.

Materials and methods; additional microscopy and spectroscopy characterization data; additional simulation results (PDF)

Movie S1 showing visualization of a 3D belted bipyramid reconstruction (MPG)

Movie S2 showing electric field enhancement calculated for belted bypyramid shown in Figure 2 (illumination wavelength, 525 nm) (MP4)

Movie S3 showing electric field enhancement calculated for ideal (nonbelted) bipyrimid (MP4)

Movie S4 showing electric field enhancement calculated for belted bypyramid shown in Figure 2 (illumination wavelength, 675 nm) (MP4)

Movie S5 shwoing electric field enhancement calculated for belted bypyramid shown in Figure 2 (illumination wavelength, 850 nm) (MP4)

Movie S5 showing Visualization of a 3D reconstruction of a chiral particle grown from a medium BP (MPG)

■ AUTHOR INFORMATION

Corresponding Author

Luis M. Liz-Marzán − *CIC biomaGUNE, Basque Research and Technology Alliance (BRTA), 20014 Donostia-San Sebastián, Spain; Centro de Investigación Biomédica en Red, Bioingeniería, Biomateriales y Nanomedicina (CIBER-BBN), 20014 Donostia-San Sebastián, Spain; Ikerbasque, 43009 Bilbao, Spain; CINBIO, Universidade de Vigo, 36310 Vigo, Spain;* orcid.org/0000-0002-6647-1353; Email: llizmarzan@cicbiomagune.es

Authors

Francisco Bevilacqua − *CIC biomaGUNE, Basque Research and Technology Alliance (BRTA), 20014 Donostia-San Sebastián, Spain*

Robin Girod − *EMAT and NANOlab Center of Excellence, University of Antwerp, B-2020 Antwerp, Belgium;* orcid.org/0000-0001-7861-7818

Victor F. Martín − *Departamento Tecnología de los Computadores y de las Comunicaciones, Universidad de Extremadura, 10003 Cáceres, Spain;* orcid.org/0000-0001-7095-7148

Manuel Obelleiro-Liz − *EM3Works, Spin-off of the University of Vigo and the University of Extremadura, 36315 Vigo, Spain;* orcid.org/0000-0003-3038-8360

Gail A. Vinnacombe-Willson − *CIC biomaGUNE, Basque Research and Technology Alliance (BRTA), 20014 Donostia-San Sebastián, Spain;* orcid.org/0000-0002-6897-6574

Kyle Van Gordon − *CIC biomaGUNE, Basque Research and Technology Alliance (BRTA), 20014 Donostia-San Sebastián, Spain*

Johan Hofkens − *Department of Chemistry, KU Leuven, 3001 Heverlee, Belgium;* orcid.org/0000-0002-9101-0567

Jose Manuel Taboada − *Departamento Tecnología de los Computadores y de las Comunicaciones, Universidad de Extremadura, 10003 Cáceres, Spain*

Sara Bals − *EMAT and NANOlab Center of Excellence, University of Antwerp, B-2020 Antwerp, Belgium;* orcid.org/0000-0002-4249-8017

Complete contact information is available at:
https://pubs.acs.org/10.1021/acsmaterialslett.4c01605

Author Contributions

F.B., J.H., and L.M.L.-M. conceptually designed the project. F.B. performed nanoparticle synthesis and analysis; K.V.G. collaborated on chiral synthesis and characterization; R.G. and S.B. performed and interpreted electron tomography measurements. V.F.M., M.O.-L. and J.M.T. performed and interpreted electromagnetic simulations. All authors contributed to writing the manuscript. CRediT: **Francisco BEVILACQUA** data curation, formal analysis, methodology, writing - original draft; **Robin Girod** data curation, formal analysis, visualization, writing - review & editing; **Victor F Martin** data curation, formal analysis, software, writing - review & editing; **Manuel Obelleiro-Liz** data curation, formal analysis, software, writing - review & editing; **Gail Anne Vinnacombe-Willson** data curation, visualization, writing - review & editing; **Kyle Van Gordon** methodology, writing - review & editing; **Johan Hofkens** conceptualization, resources, writing - review & editing; **Jose M Taboada** formal analysis, methodology, resources, software, writing - review & editing; **Sara Bals** formal analysis, funding acquisition, resources, supervision, writing - review & editing; **Luis M. Liz-Marzán** conceptualization, formal analysis, funding acquisition, methodology, project administration, resources, supervision, validation, writing - review & editing.

Notes

The authors declare no competing financial interest.

■ REFERENCES

(1) Langer, J.; Jimenez De Aberasturi, D.; Aizpurua, J.; Alvarez-Puebla, R. A.; Auguié, B.; Baumberg, J. J.; Bazan, G. C.; Bell, S. E. J.; Boisen, A.; Brolo, A. G.; Choo, J.; Cialla-May, D.; Deckert, V.; Fabris, L.; Faulds, K.; García De Abajo, F. J.; Goodacre, R.; Graham, D.; Haes, A. J.; Haynes, C. L.; Huck, C.; Itoh, T.; Käll, M.; Kneipp, J.; Kotov, N. A.; Kuang, H.; Le Ru, E. C.; Lee, H. K.; Li, J.-F.; Ling, X. Y.; Maier, S. A.; Mayerhöfer, T.; Moskovits, M.; Murakoshi, K.; Nam, J.-M.; Nie, S.; Ozaki, Y.; Pastoriza-Santos, I.; Perez-Juste, J.; Popp, J.; Pucci, A.; Reich, S.; Ren, B.; Schatz, G. C.; Shegai, T.; Schlücker, S.; Tay, L.-L.; Thomas, K. G.; Tian, Z.-Q.; Van Duyne, R. P.; Vo-Dinh, T.; Wang, Y.; Willets, K. A.; Xu, C.; Xu, H.; Xu, Y.; Yamamoto, Y. S.; Zhao, B.; Liz-Marzán, L. M. Present and Future of Surface-Enhanced Raman Scattering. *ACS Nano* **2020**, *14*, 28−117.

(2) Tadgell, B.; Liz-Marzán, L. M. Probing Interactions between Chiral Plasmonic Nanoparticles and Biomolecules. *Chem.—Eur. J.* **2023**, *29*, No. e202301691.

(3) Troncoso-Afonso, L.; Vinnacombe-Willson, G. A.; García-Astrain, C.; Liz-Márzan, L. M. SERS in 3D Cell Models: A Powerful Tool in Cancer Research. *Chem. Soc. Rev.* **2024**, *53*, 5118−5148.

(4) García-Astrain, C.; Henriksen-Lacey, M.; Lenzi, E.; Renero-Lecuna, C.; Langer, J.; Piñeiro, P.; Molina-Martínez, B.; Plou, J.; Jimenez De Aberasturi, D.; Liz-Marzán, L. M. A Scaffold-Assisted 3D Cancer Cell Model for Surface-Enhanced Raman Scattering-Based Real-Time Sensing and Imaging. *ACS Nano* **2024**, *18*, 11257−11269.

(5) Giljohann, D. A.; Seferos, D. S.; Daniel, W. L.; Massich, M. D.; Patel, P. C.; Mirkin, C. A. Gold Nanoparticles for Biology and Medicine. *Angew. Chem. Int. Ed* **2010**, *49*, 3280−3294.

(6) González-Callejo, P.; García-Astrain, C.; Herrero-Ruiz, A.; Henriksen-Lacey, M.; Seras-Franzoso, J.; Abasolo, I.; Liz-Marzán, L. M. 3D Bioprinted Tumor-Stroma Models of Triple-Negative Breast Cancer Stem Cells for Preclinical Targeted Therapy Evaluation. *ACS Appl. Mater. Interfaces* **2024**, *16*, 27151−27163.

(7) Liz-Marzán, L. M. Tailoring Surface Plasmons through the Morphology and Assembly of Metal Nanoparticles. *Langmuir* **2006**, *22*, 32−41.

(8) Gole, A.; Murphy, C. J. Seed-Mediated Synthesis of Gold Nanorods: Role of the Size and Nature of the Seed. *Chem. Mater.* **2004**, *16*, 3633−3640.

(9) Pérez-Juste, J.; Pastoriza-Santos, I.; Liz-Marzán, L. M.; Mulvaney, P. Gold Nanorods: Synthesis, Characterization and Applications. *Coord. Chem. Rev.* **2005**, *249*, 1870−1901.

(10) Scarabelli, L.; Sánchez-Iglesias, A.; Pérez-Juste, J.; Liz-Marzán, L. M. A "Tips and Tricks" Practical Guide to the Synthesis of Gold Nanorods. *J. Phys. Chem. Lett.* **2015**, *6*, 4270−4279.

(11) Chow, T. H.; Li, N.; Bai, X.; Zhuo, X.; Shao, L.; Wang, J. Gold Nanobipyramids: An Emerging and Versatile Type of Plasmonic Nanoparticles. *Acc. Chem. Res.* **2019**, *52*, 2136−2146.

(12) González-Rubio, G.; Kumar, V.; Llombart, P.; Díaz-Núñez, P.; Bladt, E.; Altantzis, T.; Bals, S.; Peña-Rodríguez, O.; Noya, E. G.; MacDowell, L. G.; Guerrero-Martínez, A.; Liz-Marzán, L. M. Disconnecting Symmetry Breaking from Seeded Growth for the Reproducible Synthesis of High Quality Gold Nanorods. *ACS Nano* **2019**, *13*, 4424−4435.

(13) Sanchez-Iglesias, A.; Winckelmans, N.; Altantzis, T.; Bals, S.; Grzelczak, M.; Liz-Marzan, L. M. High Yield Seeded Growth of Monodisperse Pentatwinned Gold Nanoparticles Through Thermally-Induced Seed Twinning. *J. Am. Chem. Soc.* **2017**, *139*, 107−110.

(14) Chateau, D.; Desert, A.; Lerouge, F.; Landaburu, G.; Santucci, S.; Parola, S. Beyond the Concentration Limitation in the Synthesis of Nanobipyramids and Other Pentatwinned Gold Nanostructures. *ACS Appl. Mater. Interfaces* **2019**, *11*, 39068−39076.

(15) Lyu, J.; Chaâbani, W.; Modin, E.; Chuvilin, A.; Bizien, T.; Smallenburg, F.; Impéror-Clerc, M.; Constantin, D.; Hamon, C. Double-Lattice Packing of Pentagonal Gold Bipyramids in Super-crystals with Triclinic Symmetry. *Adv. Mater.* **2022**, *34*, No. 2200883.

(16) Hu, J.; Li, L.; Zou, Y.; Fan, Z.; Jiang, J. Cysteine-Induced Growth of Jagged Gold Bipyramids from Penta-Twinned Nanorod Seeds. *J. Chem. Phys.* **2024**, *160*, No. 204703.

(17) Carbó-Argibay, E.; Rodríguez-González, B.; Gómez-Graña, S.; Guerrero-Martínez, A.; Pastoriza-Santos, I.; Pérez-Juste, J.; Liz-Marzán, L. M. The Crystalline Structure of Gold Nanorods Revisited: Evidence for Higher-Index Lateral Facets. *Angew. Chem. Int. Ed* **2010**, *49*, 9397−9400.

(18) Goris, B.; Bals, S.; Van Den Broek, W.; Carbó-Argibay, E.; Gómez-Graña, S.; Liz-Marzán, L. M.; Van Tendeloo, G. Atomic-Scale Determination of Surface Facets in Gold Nanorods. *Nat. Mater.* **2012**, *11*, 930−935.

(19) Liu, M.; Guyot-Sionnest, P. Mechanism of Silver(I)-Assisted Growth of Gold Nanorods and Bipyramids. *J. Phys. Chem. B* **2005**, *109*, 22192−22200.

(20) Lee, J.-H.; Gibson, K. J.; Chen, G.; Weizmann, Y. Bipyramid-Templated Synthesis of Monodisperse Anisotropic Gold Nanocrystals. *Nat. Commun.* **2015**, *6*, 7571.

(21) Pardehkhorram, R.; Bonaccorsi, S.; Zhu, H.; Gonçales, V. R.; Wu, Y.; Liu, J.; Lee, N. A.; Tilley, R. D.; Gooding, J. J. Intrinsic and Well-Defined Second Generation Hot Spots in Gold Nanobipyramids *versus* Gold Nanorods. *Chem. Commun.* **2019**, *55*, 7707−7710.

(22) Chen, H.; Kou, X.; Yang, Z.; Ni, W.; Wang, J. Shape- and Size-Dependent Refractive Index Sensitivity of Gold Nanoparticles. *Langmuir* **2008**, *24*, 5233−5237.

(23) Grzelczak, M.; Pérez-Juste, J.; Mulvaney, P.; Liz-Marzán, L. M. Shape Control in Gold Nanoparticle Synthesis. *Chem. Soc. Rev.* **2008**, *37*, 1783.

(24) Almora-Barrios, N.; Novell-Leruth, G.; Whiting, P.; Liz-Marzán, L. M.; López, N. Theoretical Description of the Role of Halides, Silver, and Surfactants on the Structure of Gold Nanorods. *Nano Lett.* **2014**, *14*, 871−875.

(25) Niu, W.; Duan, Y.; Qing, Z.; Huang, H.; Lu, X. Shaping Gold Nanocrystals in Dimethyl Sulfoxide: Toward Trapezohedral and

Bipyramidal Nanocrystals Enclosed by {311} Facets. *J. Am. Chem. Soc.* **2017**, *139*, 5817−5826.

(26) Canbek, Z. C.; Cortes-Huerto, R.; Testard, F.; Spalla, O.; Moldovan, S.; Ersen, O.; Wisnet, A.; Wang, G.; Goniakowski, J.; Noguera, C.; Menguy, N. Twinned Gold Nanoparticles under Growth: Bipyramids Shape Controlled by Environment. *Cryst. Growth Des.* **2015**, *15*, 3637−3644.

(27) Burgin, J.; Florea, I.; Majimel, J.; Dobri, A.; Ersen, O.; Tréguer-Delapierre, M. 3D Morphology of Au and Au@Ag Nanobipyramids. *Nanoscale* **2012**, *4*, 1299.

(28) Xiao, C.; Lu, B.-A.; Xue, P.; Tian, N.; Zhou, Z.-Y.; Lin, X.; Lin, W.-F.; Sun, S.-G. High-Index-Facet- and High-Surface-Energy Nanocrystals of Metals and Metal Oxides as Highly Efficient Catalysts. *Joule* **2020**, *4*, 2562−2598.

(29) Frank, U.; Drobek, D.; Sánchez-Iglesias, A.; Wawra, S. E.; Nees, N.; Walter, J.; Pflug, L.; Apeleo Zubiri, B.; Spiecker, E.; Liz-Marzán, L. M.; Peukert, W. Determination of 2D Particle Size Distributions in Plasmonic Nanoparticle Colloids via Analytical Ultracentrifugation: Application to Gold Bipyramids. *ACS Nano* **2023**, *17*, 5785−5798.

(30) Smith, J. D.; Bladt, E.; Burkhart, J. A. C.; Winckelmans, N.; Koczkur, K. M.; Ashberry, H. M.; Bals, S.; Skrabalak, S. E. Defect-Directed Growth of Symmetrically Branched Metal Nanocrystals. *Angew. Chem., Int. Ed.* **2020**, *59*, 943−950.

(31) Sow, C.; Sarma, A.; Schropp, A.; Dzhigaev, D.; Keller, T. F.; Schroer, C. G.; Sanyal, M. K.; Kulkarni, G. U. Unraveling the Spatial Distribution of Catalytic Non-Cubic Au Phases in a Bipyramidal Microcrystallite by X-Ray Diffraction Microscopy. *ACS Nano* **2020**, *14*, 9456−9465.

(32) Kang, X.; Ruan, Q.; Zhang, H.; Bao, F.; Guo, J.; Tang, M.; Cheng, S.; Wang, J. Concave Gold Bipyramids Bound with Multiple High-Index Facets: Improved Raman and Catalytic Activities. *Nanoscale* **2017**, *9*, 5879−5886.

(33) Lee, H.-E.; Ahn, H.-Y.; Mun, J.; Lee, Y. Y.; Kim, M.; Cho, N. H.; Chang, K.; Kim, W. S.; Rho, J.; Nam, K. T. Amino-Acid- and Peptide-Directed Synthesis of Chiral Plasmonic Gold Nanoparticles. *Nature* **2018**, *556*, 360−365.

(34) Ni, B.; Mychinko, M.; Gómez-Graña, S.; Morales-Vidal, J.; Obelleiro-Liz, M.; Heyvaert, W.; Vila-Liarte, D.; Zhuo, X.; Albrecht, W.; Zheng, G.; González-Rubio, G.; Taboada, J. M.; Obelleiro, F.; López, N.; Pérez-Juste, J.; Pastoriza-Santos, I.; Cölfen, H.; Bals, S.; Liz-Marzán, L. M. Chiral Seeded Growth of Gold Nanorods Into Fourfold Twisted Nanoparticles with Plasmonic Optical Activity. *Adv. Mater.* **2023**, *35*, No. 2208299.

(35) González-Rubio, G.; Mosquera, J.; Kumar, V.; Pedrazo-Tardajos, A.; Llombart, P.; Solís, D. M.; Lobato, I.; Noya, E. G.; Guerrero-Martínez, A.; Taboada, J. M.; Obelleiro, F.; MacDowell, L. G.; Bals, S.; Liz-Marzán, L. M. Micelle-Directed Chiral Seeded Growth on Anisotropic Gold Nanocrystals. *Science* **2020**, *368*, 1472−1477.

(36) Zhuo, X.; Mychinko, M.; Heyvaert, W.; Larios, D.; Obelleiro-Liz, M.; Taboada, J. M.; Bals, S.; Liz-Marzán, L. M. Morphological and Optical Transitions during Micelle-Seeded Chiral Growth on Gold Nanorods. *ACS Nano* **2022**, *16*, 19281−19292.

(37) Sun, X.; Sun, L.; Lin, L.; Guo, S.; Yang, Y.; Zhang, B.; Liu, C.; Tao, Y.; Zhang, Q. Tuning the Geometry and Optical Chirality of Pentatwinned Au Nanoparticles with 5-Fold Rotational Symmetry. *ACS Nano* **2024**, *18*, 9543−9556.

(38) Van Gordon, K.; Ni, B.; Girod, R.; Mychinko, M.; Bevilacqua, F.; Bals, S.; Liz-Marzán, L. M. Single Crystal and Pentatwinned Gold Nanorods Result in Chiral Nanocrystals with Reverse Handedness. *Angew. Chem., Int. Ed.* **2024**, *63*, No. e202403116.

(39) Carone, A.; Mariani, P.; Désert, A.; Romanelli, M.; Marcheselli, J.; Garavelli, M.; Corni, S.; Rivalta, I.; Parola, S. Insight on Chirality Encoding from Small Thiolated Molecule to Plasmonic Au@Ag and Au@Au Nanoparticles. *ACS Nano* **2022**, *16*, 1089−1101.

(40) Zhang, L.; Chen, Y.; Zheng, J.; Lewis, G. R.; Xia, X.; Ringe, E.; Zhang, W.; Wang, J. Chiral Gold Nanorods with Five-Fold Rotational Symmetry and Orientation-Dependent Chiroptical Properties of

Their Monomers and Dimers. *Angew. Chem., Int. Ed.* **2023**, *62*, No. e202312615.

(41) Fröhlich, E.; Fröhlich, E. Cytotoxicity of Nanoparticles Contained in Food on Intestinal Cells and the Gut Microbiota. *IJMS* **2016**, *17*, 509.

(42) Hanske, C.; González-Rubio, G.; Hamon, C.; Formentín, P.; Modin, E.; Chuvilin, A.; Guerrero-Martínez, A.; Marsal, L. F.; Liz-Marzán, L. M. Large-Scale Plasmonic Pyramidal Supercrystals via Templated Self-Assembly of Monodisperse Gold Nanospheres. *J. Phys. Chem. C* **2017**, *121*, 10899−10906.

(43) Hendel, T.; Wuithschick, M.; Kettemann, F.; Birnbaum, A.; Rademann, K.; Polte, J. In Situ Determination of Colloidal Gold Concentrations with UV−Vis Spectroscopy: Limitations and Perspectives. *Anal. Chem.* **2014**, *86*, 11115−11124.

(44) Jenkinson, K.; Liz-Marzán, L. M.; Bals, S. Multimode Electron Tomography Sheds Light on Synthesis, Structure, and Properties of Complex Metal-Based Nanoparticles. *Adv. Mater.* **2022**, *34*, No. 2110394.

(45) Solís, D. M.; Taboada, J. M.; Obelleiro, F.; Liz-Marzán, L. M.; García De Abajo, F. J. Toward Ultimate Nanoplasmonics Modeling. *ACS Nano* **2014**, *8*, 7559−7570.